1 **Development of the chick wing and leg neuromuscular systems and their**

2 **plasticity in response to changes in digit numbers**

3

4 Maëva Luxey[1,#], Bianka Berki[1,#], Wolf Heusermann[2], Sabrina Fischer[1], & Patrick Tschopp[1,*]

5

6 [1]DUW Zoology, University of Basel, Vesalgasse 1, CH-4051, Basel, Switzerland; [2]IMCF

7 Biozentrum, University of Basel, Basel, Switzerland

8

9 [#]Equally contributing

10

11 [*]Corresponding author: Patrick Tschopp

12   Tel.: +41 61 207 56 49

13   patrick.tschopp@unibas.ch

14

15

16

17 **RUNNING TITLE:**

18 Autopod nerve and muscle plasticity

19

20

21 **KEY WORDS:**

22 Limb musculoskeletal apparatus, Autopod evolution, Limb neuromuscular 3D-atlas, light-

23 sheet microscopy, Polydactyly, Forelimb - hindlimb differences.

24

25   **SUMMARY STATEMENT / HIGHLIGHTS:** Using light-sheet microscopy and

26   3D-nerve and -muscle reconstructions, we uncover a differential plasticity in the limb

27   neuromuscular system's ability to adapt to changes in digit numbers.

28

29 **ABSTRACT**

30   The tetrapod limb has long served as a paradigm to study vertebrate pattern formation.

31 During limb morphogenesis, a number of distinct tissue types are patterned and subsequently

32 must be integrated to form coherent functional units. For example, the musculoskeletal

33 apparatus of the limb requires the coordinated development of the skeletal elements,

34 connective tissues, muscles and nerves. Here, using light-sheet microscopy and 3D-

35 reconstructions, we concomitantly follow the developmental emergence of nerve and muscle

36 patterns in chicken wings and legs, two appendages with highly specialized locomotor

37 outputs. Despite a comparable flexor/extensor-arrangement of their embryonic muscles,

38 wings and legs show a rotated innervation pattern for their three main motor nerve branches.

39 To test the functional implications of these distinct neuromuscular topologies, we challenge

40 their ability to adapt and connect to an experimentally altered skeletal pattern in the distal

41 limb, the autopod. Our results show that, unlike autopod muscle groups, motor nerves are

42 unable to fully adjust to a changed peripheral organisation, potentially constrained by their

43 original projection routes. As the autopod has undergone substantial morphological

44 diversifications over the course of tetrapod evolution, our results have implications for the

45 coordinated modification of the distal limb musculoskeletal apparatus, as well as for our

46 understanding of the varying degrees of motor functionality associated with human hand and

47 foot malformations.

48

INTRODUCTION

During vertebrate limb development, growth and patterning need to be precisely orchestrated in both space and time. Genetic analyses and experimental embryology studies have revealed the existence of multiple cross-regulatory signaling systems that confer developmental stability, while at the same time leave room for evolutionary modifications to occur therein (Zeller et al., 2009; Suzuki, 2013; Petit et al., 2017). This task, however, is complicated by functional units inside the limb that consist of multiple tissue types, some of which originate from different embryonic precursor pools. For example, skeletal cells of the limb musculoskeletal apparatus originate from lateral plate mesoderm precursors (Gilbert, 2010). Somite-derived muscle cells migrate into the limb bud, form distinct muscle groups and attach to the developing skeletal elements *via* tendons (Chevallier et al., 1977; Kardon, 1998; Schweitzer et al., 2010; Sharir et al., 2011; Francisco Botelho et al., 2015). Motor neurons residing in the spinal cord, and sensory neurons in the dorsal root ganglia, project their axons into the limb periphery to connect to these muscles in a highly stereotypical manner (Landmesser, 1978; Landmesser, 2001; Bonanomi, 2019). Hence, embryonic patterning of these three tissues needs to be tightly coordinated, to successfully integrate skeletal, muscular and neural anatomy, and produce a fully operational limb. Likewise, evolutionary modifications in the pattern of any one of these tissues necessitate parallel alterations in the morphology of the others.

Over the course of vertebrate evolution, the skeleton of tetrapod limbs has greatly diversified, reflecting adaptations to a variety of different styles of locomotion. In the proximal parts of the limb the number of skeletal elements is largely conserved, with evolutionary modifications occurring predominantly through changes in length and girth of the respective bones (Kronenberg, 2003; Hall, 2015). Such alterations can be apparent even within a single species, due to different locomotor behaviours associated with the respective fore- and hindlimbs (Cooper, 2011; Wimsatt, 2012; de Bakker et al., 2013). The most striking differences, however, have appeared in the skeleton of the autopod, with changes occurring in both digit patterns and numbers (Wagner and Chiu, 2001; Richardson and Chipman, 2003). Based on seminal work in traditional model organisms, we now have the ability to elucidate these evolutionary autopod diversifications at the molecular level (Zuniga, 2015; Petit et al., 2017). For example, variations in Sonic Hedgehog signalling pathway activity have been demonstrated to affect digit numbers in a wide range of tetrapod species (Shapiro et al., 2003; Lettice et al., 2008; Cooper et al., 2014; Lopez-Rios et al., 2014). The resulting

82 morphological changes in the autopod, however, have so far mainly been studied at the

83 skeletal level, while muscle and nerve modifications in experimentally altered limbs have

84 only been described at more proximal levels (Stirling and Summerbell, 1988; Duprez et al.,

85 1999).

86 Here, capitalizing on the power of whole-mount immunohistochemistry and light-sheet

87 fluorescent microscopy (LSFM), we present a 3D-atlas of the developing neuromuscular

88 system in distal chicken limbs. While early muscle patterning occurs in a largely uniform

89 dorso-ventral manner, we find a relative rotation of the main motor nerves between wings

90 and legs. By experimentally altering the skeletal formula of the autopod, we challenge the

91 developmental plasticity of these two distinct neuromuscular architectures to adapt to

92 changes in dactyly. Intriguingly, we find that while the musculature closely follows changes

93 in skeletal topology, wing and leg innervation patterns are only partially responsive. This

94 apparent discrepancy in patterning flexibility, between the muscular and nervous systems, has

95 implications for the evolutionary diversification of the vertebrate autopod, as well as for the

96 different congenital malformations affecting human hands and feet.

97

RESULTS AND DISCUSSION

3D-analysis of neuromuscular development in chicken limbs

In order to monitor the coordinated patterning of nerves and muscle groups, we first produced a 3D-atlas of the developing neuromuscular system in chicken fore- and hindlimbs. Through whole-mount double-immunohistochemistry against neuron-specific intermediate filament protein (neurofilament, '*NF200*') and muscle-specific myosin heavy chain (MHC, '*MF20*'), we visualized the appearance of limb nerves and muscle groups, respectively. Following CUBIC clearing, LSFM image acquisition and 3D-reconstruction (Susaki et al., 2014; Belle et al., 2017), segmentation-based tracing was used to delineate and pseudo-colour major nerves and muscle bundles (Fig. 1A,B; Fig. S1A,B; Fig. S2A,B). Using this experimental workflow, we produced a developmental time-series for both wing and leg, spanning stages Hamburger-Hamilton (HH) HH26 to HH36 (day 5 to day 10 of development; Hamburger and Hamilton, 1951) (Fig. 1C,D; Fig. S1C-F; Fig. S2C-F; Movie 1 and 2).

At day 5 of development in the wing, growing axons are invading the bud and form two main fascicles, one dorsal (n. brachialis superior) and one ventral (n. brachialis inferior) (data not shown). Around day 6, further subdivisions become evident, giving rise to the three major nerve branches of the limb that contain the projecting axons of motor and sensory neurons: the radial nerve (cyan) on the dorsal side; the median (yellow) and ulnar nerve (magenta) on the ventral side. From there, the branches split further to innervate in a stereotypical and non-overlapping manner the musculature of the forming digit territories, which become visible at later time-points (day 7 to day 10) (Fig. 1C, Fig. S1C,E). Three main nerve branches also connect to the leg musculature. Dorsally, two arched nerves, the median (green) and lateral (orange) fibulars, share a common peroneal origin (Fig. S2C). On the ventral side, innervation of the foot is provided by the plantar nerve (Fig. S2E, purple).

In parallel to limb innervation, muscle precursors aggregate and differentiate into dorsal and ventral muscles masses, soon after their migration from the dermomyotome (Schramm and Solursh, 1990; Hayashi and Ozawa, 1995) (data not shown). These two masses then split along the antero-posterior (A/P) and proximo-distal (Prox./Dist.) axes to form the individual muscles of the wing and the leg (Fig. 1D; Fig. S1D,F; Fig. S2D,F). At day 6, the hand/foot muscles masses are still continuous with the forearm/shank that has started to cleave along its A/P axis. From day 7 onwards this connection is progressively lost, with a spatial detachment of the forearm/shank and hand/foot muscles masses at the intermediate tendon primordia levels (Kardon, 1998). Starting around the same stage, discrete hand and foot muscles

131 separate anteriorly-posteriorly from their primary muscle masses. Those muscles become
132 increasingly individualized, elongate and adopt their eventual fusiform shape from day 8 to
133 day 10. As such, they give rise to a precise muscular topology, with eleven main muscles in
134 the wing autopod and seven in the foot (Fig. S3A-D). At similar developmental stages both
135 muscle individualization and peripheral nerve branching appear more advanced in the
136 hindlimb than in the forelimb. These observations support the notion that a developmental
137 heterochrony may exist between embryonic chicken limbs, with the development of legs
138 being slightly more advanced then in wings (Bininda-Emonds et al., 2007). Collectively, we
139 present a comprehensive 3D-atlas of the developing neuromuscular system in chicken wings
140 and legs at high spatial and temporal resolution.

141 **Differential innervation patterns between the wing and the leg**

142 Although both fore- and hindlimbs display three major motor axon-containing nerve
143 branches, their A/P and D/V (dorso-ventral) layouts show striking differences. Namely, while
144 a single nerve (radial, cyan) occupies the anterior-dorsal quadrant of the wing cross-section,
145 this arrangement is inverted for the plantar nerve (purple) in the posterior-ventral sector of
146 the leg (Fig. 2A,B). The median-ulnar (yellow, magenta) and median fibular-lateral fibular
147 (green, orange) nerve pairs reside in the ventral and dorsal halves of the wing and leg,
148 respectively. These distinct nerve arrangements are unlikely to result from the different
149 rotations of the adult limbs, relative to the main body axis, as at the time of nerve invasion
150 the orientations of fore- and hindlimbs are identical. Accordingly, dorsal wing and leg
151 extensor muscles are predominantly innervated by either single (wing) or double (leg) nerve
152 branches, with the ventrally located flexors displaying the opposite configuration (Fig. 2C).
153 In addition to differences in nerve branch arrangements along the A/P and D/V axes, the
154 single nerves in the wing and the leg also display distinct A/P projection routes. While the
155 radial nerve follows a distal curvature reaching from the anterior to the posterior side of the
156 dorsal wing, the ventral plantar nerve takes an opposite trajectory, posterior to anterior in the
157 foot (Fig. 2D,E). Moreover, both paired nerves, median-ulnar ventrally in the wing and
158 median fibular-lateral fibular dorsally in the leg, fuse and produce an arched structure whose
159 location coincides with the proximal onset of the respective autopod muscle groups (Fig.
160 2D,E; arrows). Hence, these results illustrate an inverted configuration for the basic
161 innervation patterns of the chicken wing and the leg (Fig. 2B, Movie 3). Such an inverted
162 arrangement of the major nerve branches in wings and legs also suggest a differential pre-
163 disposition in their ability to respond and adapt to changes in skeleton and/or muscle
164 anatomy.

Innervation plasticity in polydactyl wings and legs

Limb innervation patterns develop in highly stereotypical fashion. Their ability to adapt to skeletal changes has been previously evaluated at proximal limb levels (Lance-Jones and Landmesser, 1981; Stirling and Summerbell, 1988). Based on these pioneering studies, we decided to re-visit this apparent plasticity of limb nervous system. We capitalized on the superior resolution offered by LSFM, and decided to focus on the distal limb, the autopod, i.e. the site of major evolutionary alterations and fine motor skills control. In order to challenge the system with extra digits, we took advantage of the chick limb model (Davey et al., 2018) using a well-established model of vertebrate polydactyly. At day 3 of development, we implanted retinoic acid-soaked beads at the anterior margin of the developing limb. This experimental manipulation is known to lead to mirror-image duplications in limb skeletal patterns, *via* the ectopic induction of *Shh* expression anteriorly (Tickle et al., 1982; Pickering et al., 2017) (Fig. S4). For autopods showing complete (wing) or partial (leg) mirror duplication, the effects on axonal pathfinding and muscle patterning were evaluated using the same staining and imaging procedures as described above.

Three days after bead implantation in the wing (day 6), both radial and median nerves seem affected and show important defasciculations at anterior-distal levels (Fig. 3A,B, arrow). The ulnar nerve, however, remains unchanged (Fig. 3B). At later stages (day 7 to day 9), we observe a complete bifurcation of the radial and median nerves, which now have invaded the polydactyl territory (Fig. 3B,C asterisks; Fig. S5A,B). At hindlimb levels, the first signs of nerves branching toward the extra digit territory also appear three days after bead implantation. The posteriorly located lateral fibular nerve is not affected, reminiscent of the fate of the ulnar nerve in the polydactyl wing (Fig. 3D-F). The anterior median fibular nerve branch, however, defasciculates and invades the anterior duplicated side, similar to the wing median nerve. Additionally, it forms an arched structure onto itself (Fig. 3E,F, arrowheads; Fig. S5C,D). In the ventral side of the polydactyl foot, the plantar nerve extends slightly further into the anterior part, with a more pronounced distal-to-proximal curvature than in controls (Fig. S5C,D), yet it does not split in response to the anterior addition of an extra digit. Surprisingly, however, an ectopic projection from the lumbosacral plexus invades the anterior margin of the hindlimb field. At later stages, the plantar nerve and the ectopic projection meet distally and form an arch from which additional branches project to the duplicated digits, in a pattern similar to control limbs (Fig. 3E,F, arrow; Fig. S5C,D).

To assess the neuronal nature of these ectopic projections in polydactyl wings and legs, we performed immunohistochemistry to discriminate motor from sensory nerves. We employed

199   a triple labeling approach, using a pan-neuronal (beta-tubulin, '*Tuj1*'; (Belle et al., 2017;
200   Friocourt et al., 2017) and a sensory neuron marker (transient adhesion glycoprotein-1, '*Tag-*
201   *1*'; (Ruegg et al., 1989; Karagogeos et al., 1997; Belle et al., 2017) , together with a muscle-
202   specific staining (fast Myosin Heavy-Chain, '*MyHC*'). This combination allowed us to
203   distinguish motor from sensory neurons, as the projections of the former stained strongly for
204   *Tuj1*, but were largely devoid of *Tag-1*, when exiting the lateral motor column (LMC) of the
205   spinal cord (Fig. S6A). At proximal levels, in both native and duplicated autopod sides, we
206   found evidence of innervation by motor as well as sensory axons (Fig. 3G-J). Importantly,
207   nerves inside of muscles bundles stained predominantly with *Tuj1* only, indicating that they
208   were made of motor axons coming from the LMC (Fig. 3G-J, arrowheads). At more distal
209   levels, i.e. beyond the autopod musculature, as well as inside the skin, only *Tuj1/Tag-1*
210   double-positive sensory nerves were detected (Fig. S6A,B).

211   Hence, in polydactyl fore- and hindlimbs, supernumerary digits are innervated by both
212   motor and sensory neurons, along ventral and dorsal routes, through defasciculation and
213   eventual nerve bifurcations at the level of the developing mesopod. This suggests the
214   presence of an additional A/P "choice point" in the limb periphery, to ensure digit-specific
215   innervation patterns (Bonanomi, 2019). Moreover, the response to such putative guidance
216   signals seems plastic and can be modulated by the presence of additional digit territories.
217   However, only two of the three major nerves seem responsive to project to the extra digits.
218   Therefore, and in contrast to the symmetric addition of skeletal elements in polydactyl wings
219   (Tickle and Towers, 2017), the corresponding innervation patterns do not represent a full
220   mirror-image duplication.

221   **Differential response of muscle and nerve patterns to a polydactyl autopod**
222   **environment**

223   We next analyzed the resulting changes in muscle patterns in polydactyl fore- and
224   hindlimbs. Since alterations in the forearm musculature have been previously reported
225   (Duprez et al., 1999), we again focused our attention on the impact of wing and leg digit
226   duplications on the respective autopod muscle groups. In both situations, three days after
227   bead implantation, the extensor and flexor masses appear expanded and the muscles fibers re-
228   orient themselves towards the native and duplicated digit territories. At later stages (day 7 to
229   day 8-9), we first observed the appearance of partial, supernumerary splits in the expanded
230   muscles masses. These splits eventually resolve into completely individualized extra muscle
231   bundles, regardless of whether a true mirror-duplication of the skeletal structure (wing) or the
232   addition of a single anterior digit (leg) occur (Fig. 4A-F).

233   In case of the duplicated wing, the morphology of these additional muscles allows for the

234   identification of their homeotic identities, which closely follow the underlying skeletal

235   topology (Fig. 5A,B). As a result, duplicated posterior-ventral muscles are now ectopically

236   contacted by the anterior split branch of the median nerve, instead of the ulnar. Thereby, they

237   have altered their connectivity to the spinal cord compared to the native, control-side

238   counterparts (e.g. FDQ', Fig. 5B; Fig. 3C,H). For the leg, the partial duplication of the

239   autopod skeleton complicates a clear muscle identity assignment. As for the wing, however, a

240   pair of ectopic muscles appears – one dorsal, one ventral to the anterior extra digit (Fig.

241   5C,D). Hence, unlike for the nervous system, all extra digits in wings and legs are matched

242   with corresponding, additional muscle bundles, thereby perfectly complementing the skeletal

243   alterations at the level of the musculature.

244   To follow the temporal dynamics of these extensive reorganizations, and estimate the

245   potential variability associated with, we assessed muscle and nerve alterations along our

246   experimental time lines. We followed muscle changes at the level of splitting and

247   individualization, whereas nerves were scored for defasciculations, bifurcations and potential

248   ectopic fusions. Plotting these results along spatiotemporal axes revealed a posterior-to-

249   anterior sequence of muscle maturation in the wing, which is recapitulated on the mirror-

250   duplicated side (Fig. 5E). A similar trend can be observed for the leg musculature, and both

251   duplicated sides in wings and legs show a slight developmental delay compared to their

252   native counterparts (Fig. 5E,F). At the innervation level, the first visible signs of nerve re-

253   arrangements appear roughly a day earlier than for the musculature, and the two most

254   posterior branches, the ulnar (wing) and the lateral fibular (leg), remain unaffected

255   throughout development (Fig. 5G,H). Thus, as for the final pattern alterations, the underlying

256   spatiotemporal dynamics are different between nerves and muscles, indicating that they are

257   subject to distinct patterning mechanisms.

258   Collectively, we report differences in the developmental plasticity of the autopod

259   neuromuscular system in response to additional digits. On the one hand, muscle groups seem

260   perfectly able to adapt their patterning to ectopic cues in the polydactyl autopod (e.g. muscle

261   connective tissue and tendon attachment sites), refine their shapes accordingly and connect to

262   the underlying skeletal elements (Fig. 5I,K) (Schweitzer et al., 2010; Diogo et al., 2015;

263   Huang et al., 2015; Vallecillo-García et al., 2017). Invading nerves, on the other hand, show

264   less flexibility in their response to autopod alterations (Fig. 5J,L). They seem constrained by

265   their projection routes, i.e. from where they send axons into the limb periphery, and remain

266   attached to their cell bodies in the developing spinal cord (Bonanomi, 2019). Importantly, not

267 only does this physical connection to the spinal cord restrict these nerves sterically, but it also
268 shapes the molecular make-up of their growth cones *via* spinal cord-intrinsic patterning
269 systems (di Sanguinetto et al., 2008; Gouti et al., 2015; Bonanomi, 2019). As such, it
270 modulates the extent to which growing nerves can respond to alterations in peripheral axon
271 guidance molecules. From an evolutionary perspective, our results thereby imply the
272 presence of distinct developmental constraints, due to the need for coordinated patterning
273 alterations in all components of the limb musculoskeletal apparatus. Namely, the fact that
274 nerve projection routes are not entirely dependent on peripheral cues will impose functional
275 patterning barriers that may prevent certain autopod morphologies from being realized.
276 Moreover, the rotated configuration we describe for fore- and hindlimb innervation patterns
277 highlights that any discussion of serial homology and individualization of tetrapod limbs
278 should not focus exclusively on skeletal elements, but consider the entire musculoskeletal
279 apparatus as a functional unit (Shubin et al., 1997; Young and Hallgrímsson, 2005; Wagner,
280 2014). From a medical point of view, our findings offer a conceptual framework to
281 understand the varying degrees of motor abilities observed in different forms of human hand
282 and foot polydactylies (Askari et al., 2016; Mehring et al., 2019).
283

284

MATERIAL AND METHODS

Experimental polydactyly

Fertilized chicken eggs (Gallus gallus domesticus) were purchased from local vendors in Switzerland. Eggs were incubated, opened and staged according to standard protocols (Hamburger and Hamilton, 1951; Ros et al., 2000). AG1-X2 resin (BioRad laboratories) were derivatised with formic acid and washed in water to adjust the pH around 4.5-5. They were then soaked in all-*trans*-retinoic acid (1 mg/ml dissolved in DMSO, Sigma) for at least 20 min at room temperature and washed in DMEM with phenol red (GIBCO™ GlutaMax), before being grafted into the anterior-distal margin of chick wing or leg buds at day 3 of development (HH19) (see Tickle et al., 1985; Ros et al., 2000). Polydactyl embryos were dissected after 3 to 6 days post implantation. In total, we analysed 19 polydactyl wings with mirror digit duplication and 12 legs with an extra digit.

Whole-Mount immunostaining and tissue clearing

Embryos were dissected and immediately fixed in Dent's fix (4:1 Methanol:DMSO) for at least one week and stored at -20°C until immunostaining. To remove pigmentation and increase signal-to-noise ratio, we bleached the dissected embryos overnight at 4°C in Dent's bleach solution (4:1:1; Methanol:DMSO:hydrogen peroxide) (Kardon, 1998). The following day, samples were re-rehydrated in decreasing MeOH/PBT (1x PBS-1%, Triton X-100) series, washed 2 times in PBT and then blocked for one hour in PBT-5% DMSO-5% sheep serum (blocking solution) at room temperature on a shaker. For double-immunostaining, samples were incubated in blocking solution with primary antibodies against neurofilament (*NF200*, Sigma, dilution 1:500) and muscle specific myosin heavy chain (*MF20*, DSHB, dilution 1:100) and placed at 4°C, with rotation for 2 nights. This was followed by one-hour washes in PBT along the day. Next, samples were incubated in secondary antibodies (α-mouse AF488 and α-rabbit Cy3; Jackson ImmuResearch, dilution 1:500) diluted in blocking solution for 2 nights at 4°C. After 6 washes of one hour in PBT at room temperature, samples were quickly washed 2 times in 1x PBS before clearing. Tissue clearing was carried out with CUBIC method as described previously (Susaki et al., 2015). Briefly, samples went through delipidation in CUBIC 1 solution followed by 2% agarose embedding and 48h incubation in CUBIC 2 solution before imaging.

Light-sheet microscopy

316   Images were acquired on a ZEISS lightsheet Z1 microscope using the Zen 2014 software

317   (ZEISS). The lightsheet was generated by lasers (wavelength 488nm and 561nm) and dual

318   side illumination was applied (Illumination optics Lightsheet Z.1 5×/0.1 ZEISS). Fluorescent

319   signals were detected with 5X air detection objectives for clearing chambers (Lightsheet Z.1

320   detection optics 5×/0.16 clearing, n=1.45, ZEISS) and acquired with PCO.Edge sCMOS

321   cameras (liquid cooled, 1920 x 1920 pixels, 16-bit readout). Stained and cleared samples

322   were submerged in a chamber filled with CUBIC 2 solution. Tiles were defined with

323   TileScan (ZEISS) for big samples, step size was optimized by Zen. All images were acquired

324   in 16-bit.

325   **3D imaging and image processing**

326   After acquisition, Zeiss .czi light-sheet microscopy files for all tiles, were loaded in

327   ArivisVision4D (Arivis) and stitched together. All planes were exported (.tiff) and loaded in

328   Imaris 9.1.2 (Bitplane) to create an Imaris file (.ims) and to carry out further analyses. 3D

329   volumes were created, nerves and muscles were segmented by thresholding and surfaces

330   were created with the Imaris "surface" plug-in. Main nerves were identified and pseudo

331   colored (Labels) for visualization purposes. At later stages, surface rendered nerves

332   innervating the skin were removed manually. Optical slices were obtained with the Imaris

333   "Ortho Slicer" and "Oblique Slicer" plug-ins. To visualize the shape of the limbs after

334   surface rendering, the gamma was set to 2 and the maximum value was set high. Images

335   (.tiff) and videos were created with Imaris "snapshot" and "animation" plug-ins. For figures,

336   separate images of the surface rendered data and the shape of the limbs were taken and

337   superposed in Fiji (Schindelin et al., 2012). Movies, created in Imaris, were put side-by-side

338   and captions were added in Adobe Premier Pro 2017 (Adobe® Creative Cloud®).

339   **Phenotypic scoring of polydactyl limbs**

340   For phenotypic scoring of polydactyl limbs, we selected only wings showing mirror-image

341   duplications with 43234 or 432234 digit formulas, and legs with five digits. Changes in

342   muscle patterning were scored as 'partial', i.e. differential fiber orientation and elongation at

343   the tip of the bundle (color code = light green, Fig. 5E,F; see e.g. 'Day 7' in Fig. 4B) or

344   'complete', i.e. individualization of muscle bundles into their characteristic shapes (color

345   code = dark green, Fig. 5E,F; see e.g. 'Day 9' in Fig. 4B) Likewise, we classified alterations

346   in nerve projection routes into two categories: 'defasciculation' (color code = light blue, Fig.

347   5G,H; see e.g. arrow in Fig. 3B) or 'complete split' (color code = dark blue, Fig. 5G,H; see

348   e.g. asterisks in Fig. 3B). Moreover, we assessed the emergence of the ectopic projection in

349   the leg (light blue = proximally restricted, dark blue = distally extended), its potential fusion

350 with the plantar nerve (dark blue), as well as the fusion of the median fibular with itself,

351 (light blue = partial, dark blue = complete).

352 **Immunostaining on cryosections**

353 Embryonic tissues were fixed in 4% PFA, cryoprotected in sucrose and sectioned at 20μm

354 thickness. Immunohistochemistry was performed using standard protocols (Tschopp et al.,

355 2014). Samples were stained with primary antibodies against *Tuj-1* (mouse, MMS-435P,

356 3μg/ml concentration, Covance), *Tag1* (rabbit, kind gift of E. Stoeckli, dilution 1:1000,

357 (Ruegg et al., 1989)) and fast Myosin Heavy-Chain (MyHC) conjugated to Alkaline

358 Phosphatase (mouse, A4335; MY32-AP; dilution 1:100; Sigma) in order to visualize all

359 neuron fibers, sensory nerves and skeletal muscles, respectively. Stainings were revealed

360 using fluorescent secondary antibodies (1:500, Jackson ImmunoResearch) or NBT/BCIP

361 reactions.

362 **Confocal microscopy**

363 Confocal images were acquired on an Olympus FLUOVIEW FV3000, using either

364 10x/0.4 (air, ApoPlan, Olympus) or 60x/1.3 (silicon oil immersion ApoPlan, Olympus)

365 objectives. Continuous laser beams were generated at 488nm and 647nm wavelength (OBIS,

366 Coherent). For 10x overviews, tiled images were stitched in Fiji (Preibisch et al., 2009). All

367 images were globally adjusted for contrast and brightness using ImageJ.

368

COMPETING INTERESTS

380 The authors declare that they have no competing interests.

381
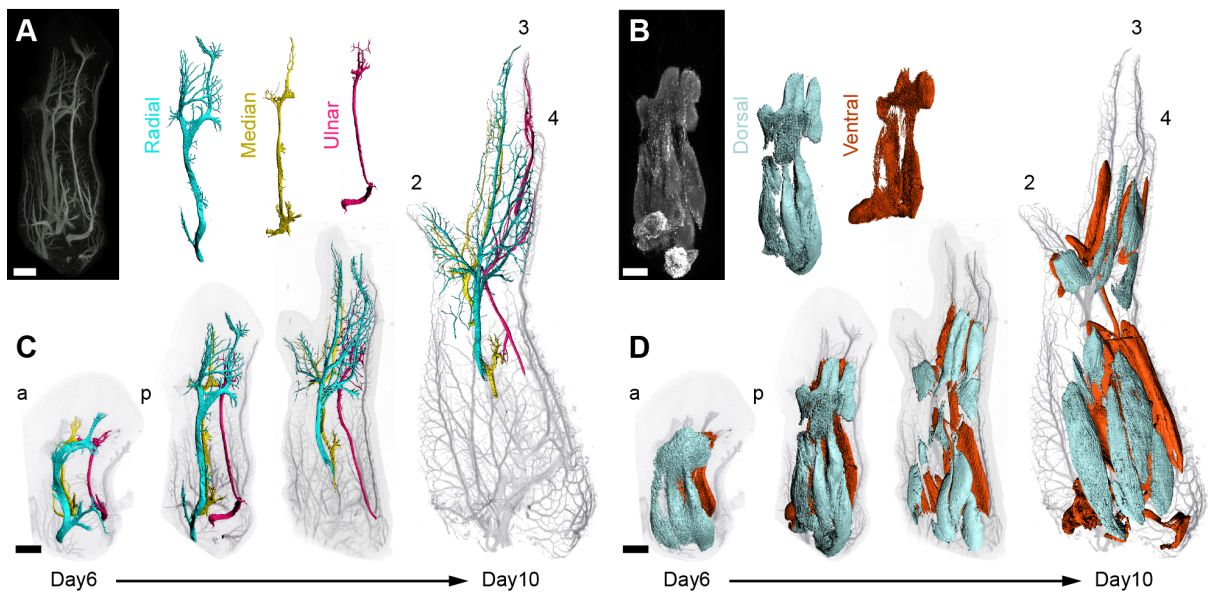
FIGURES

Figure 1: 3D-analysis of the developing neuromuscular system in the chicken forelimb

(A, B) Image acquisition and analysis workflow used to identify nerves innervating the autopod and its corresponding muscle masses. Nerves and muscles were visualized with antibodies against neurofilament (*NF200*) and myosin heavy chains (*MF20*) and imaged with a light sheet microscope. After 3D reconstruction of the embryonic wings, surfaces were rendered using segmentation-based tracing to highlight structures of interest. The radial nerve (cyan) innervates the dorsal muscle mass (light blue), while the median nerve (yellow) anteriorly and the ulnar nerve (magenta) posteriorly connect to the ventral muscle mass (red). (C,D) Dorsal view of the neuromuscular development in the wing between day 6 and day 10 of development. In this time window, motor and sensory axons invade the developing wing and simultaneously muscle bellies segregate from dorsal and ventral muscle masses. The radial nerve innervates all three digits in the dorsal part whereas ventrally, the median arborizes into digit 1 and digit 2 and the ulnar in digit 2 and 3. A/P, anterior/posterior, Prox./Dist., proximal/distal. After day 7, limbs were cropped at zeugopod levels, to allow visualization of the intermediate tendon primordia location (forearm-hand junction). Scale bars represent approx. 500μm.
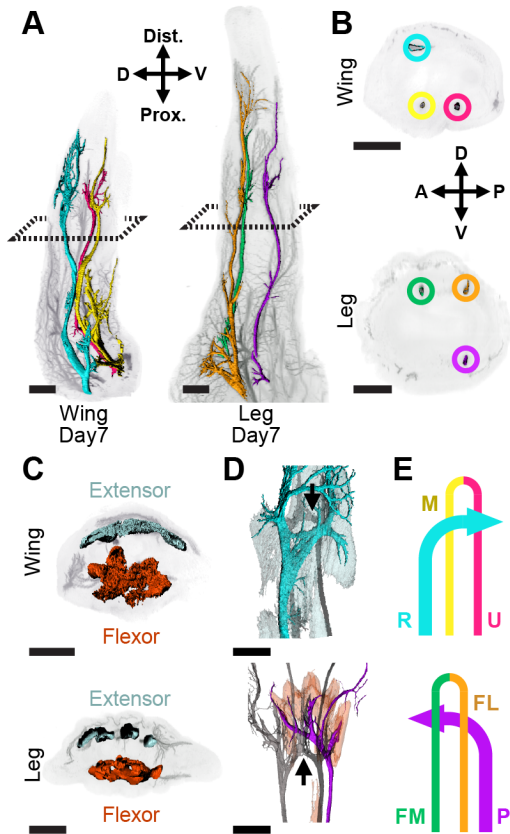
Figure 2: Differential innervation patterns in chicken wings and legs

(A,B) Side views (A) and virtual cross sections (B) of the nervous systems at the indicated levels (A, dashed lines) of a 3D-reconstructed wing and leg at day 7 of development. Three main motor axon-containing nerves project into both wing and leg. In the wing, we find one dorsal-anterior (Radial, cyan) and two ventral nerves (Median and Ulnar, yellow and magenta). In the leg, one nerve (Plantar, purple) can be found posterior-ventrally, while two nerves (Median fibular and Lateral fibular, green and orange) innervate the dorsal musculature. (C) Virtual cross sections of the muscle masses at the autopod level at day 7 of development. In both wing and leg, dorsal and ventral masses give rise to extensor and flexor muscles, respectively. (D,E) Dorsal views (D) and schematics (E) of wing and leg innervation patterns. In the wing, the dorsal radial nerve reaches all extensor muscles by projecting from anterior to posterior, while the ventral plantar nerve innervates flexor muscles by turning from posterior to anterior in the leg. The paired nerve branches, ventral in the wing and dorsal in the leg, fuse distally to from an arched structure (D, arrow). D/V, dorsal/ventral, Prox./Dist., proximal/distal; A/P, anterior/posterior. R, radial nerve; M, median nerve; U, ulnar nerve; FM, medial fibular; FL, lateral fibular; P, plantar. Scale bars represent approx. 500µm.
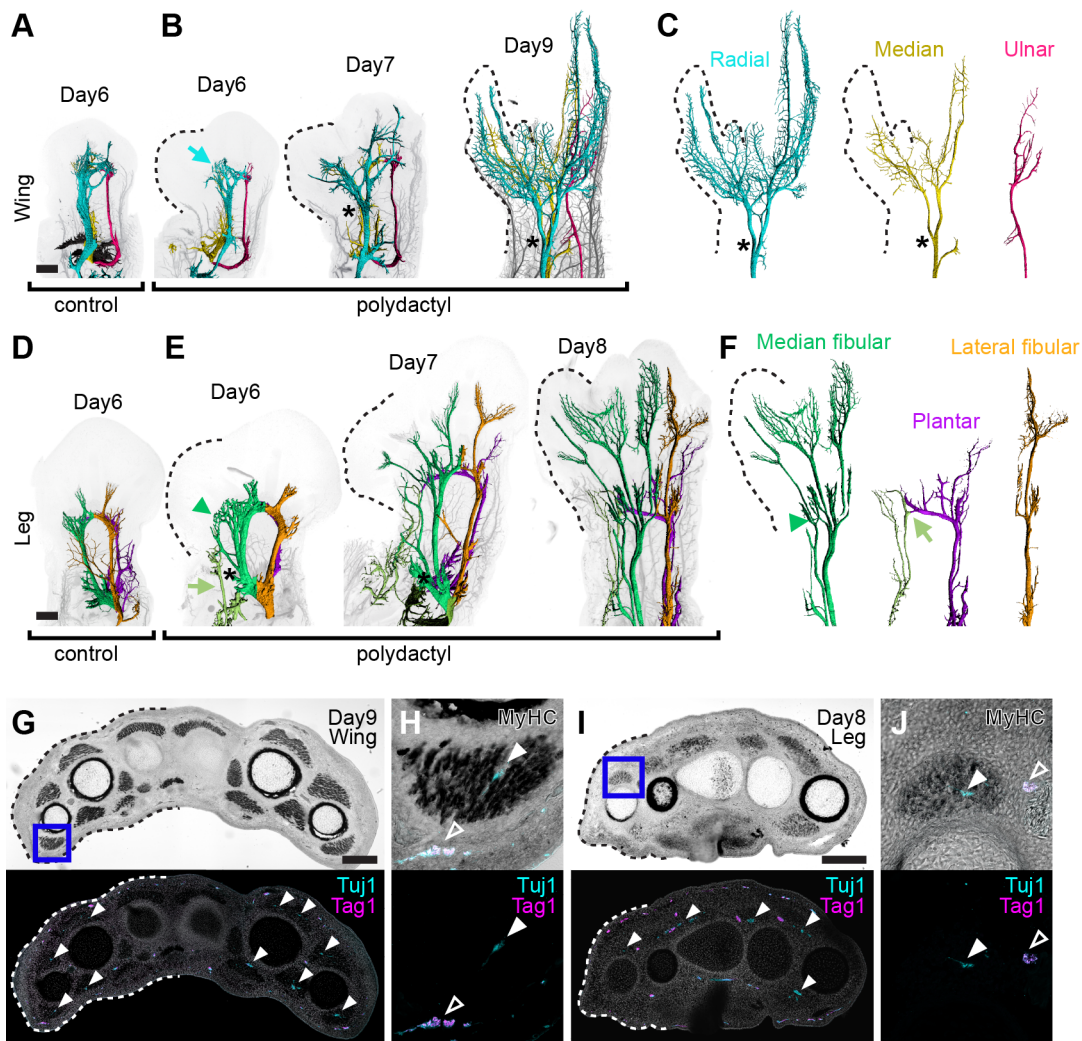
Figure 3: Modified motor and sensory innervation patterns in polydactyl wings and legs

(A-C) Dorsal view of developmental progression of innervation patterns in control (A) and polydactyl wings (B). An arrow highlights the early defasciculation of the radial nerve (B), with the median following approximately one day later. Asterisks mark the ectopic bifurcation points of the respective nerves. The overall pattern of the ulnar nerve does not seem to be affected by the polydactyly (B,C). Both radial and median nerves bifurcate and innervate the duplicated digit territories (C, dotted lines). (D-F) Dorsal view of developmental progression of innervation patterns in control (D) and polydactyl legs (E). The median fibular nerve defasciculates to innervate the dorsal half of the extra digit, and forms a persistent arched structured with itself (E,F; arrows). In the ventral portion of the leg, an ectopic projection (E,F, olive green) emerges and fuses with the plantar nerve into an additional arch (F, arrowhead). The lateral fibular nerve does not respond to the presence of an extra digit. (G-J) Innervation of extra digit territories by both motor and sensory neurons

18

444   in polydactyl wings (G,H) and legs (I,J). Motor axon projections inside muscle bundles stain

445   for *Tuj1* only (G-J, arrowheads), whereas as sensory nerves are *Tuj1/Tag-1* double-positive

446   (H,J, empty arrowheads). Blue boxes in (G,I) corresponds to magnified views of the FDQ'

447   and d_a muscles in (H,I), respectively (see Fig. 5B,D for muscles nomenclature). All images

448   anterior to the left, dotted lines demarcate polydactyl sides. Scale bars represent approx.

449   500μm in A-F, 250μm in G,I.

450

451
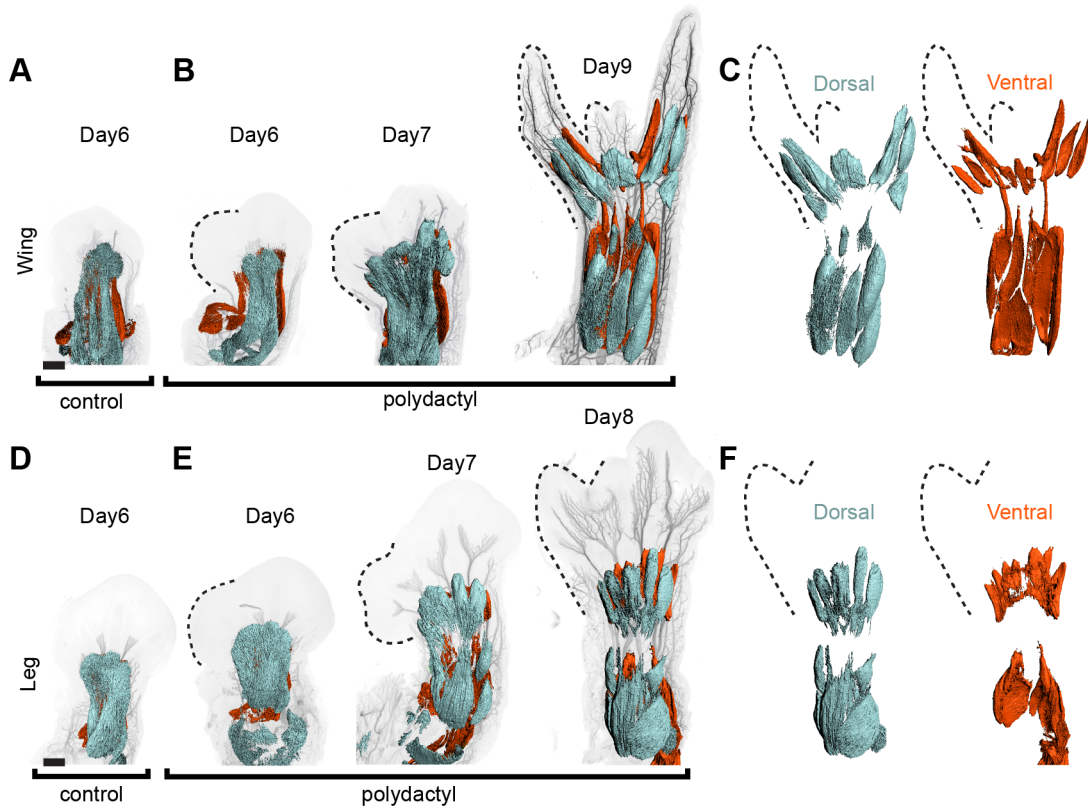
Figure 4: Modified muscle development in wing and leg polydactylies

(A-F) Dorsal view of muscle development in control and polydactyl wings (A-C) and legs (D-F). At day 6, distal muscle masses are expanded along the anterior-posterior axis, and start to split at around day 7 (B). At day 9, wing dorsal (extensor, blue) and ventral (flexor, red) muscles are completely split and individualized into a complete mirror-duplicate pattern and connect to all digits in both native and duplicated halves of the autopod (dotted lines, C). Likewise, similar dynamics lead to all native and extra digits in the foot being matched by dorsal (extensor, blue) and ventral (flexor, red) muscle groups (dotted lines, F). All images anterior to the left, distal on top. Scale bars represent approx. 500μm.
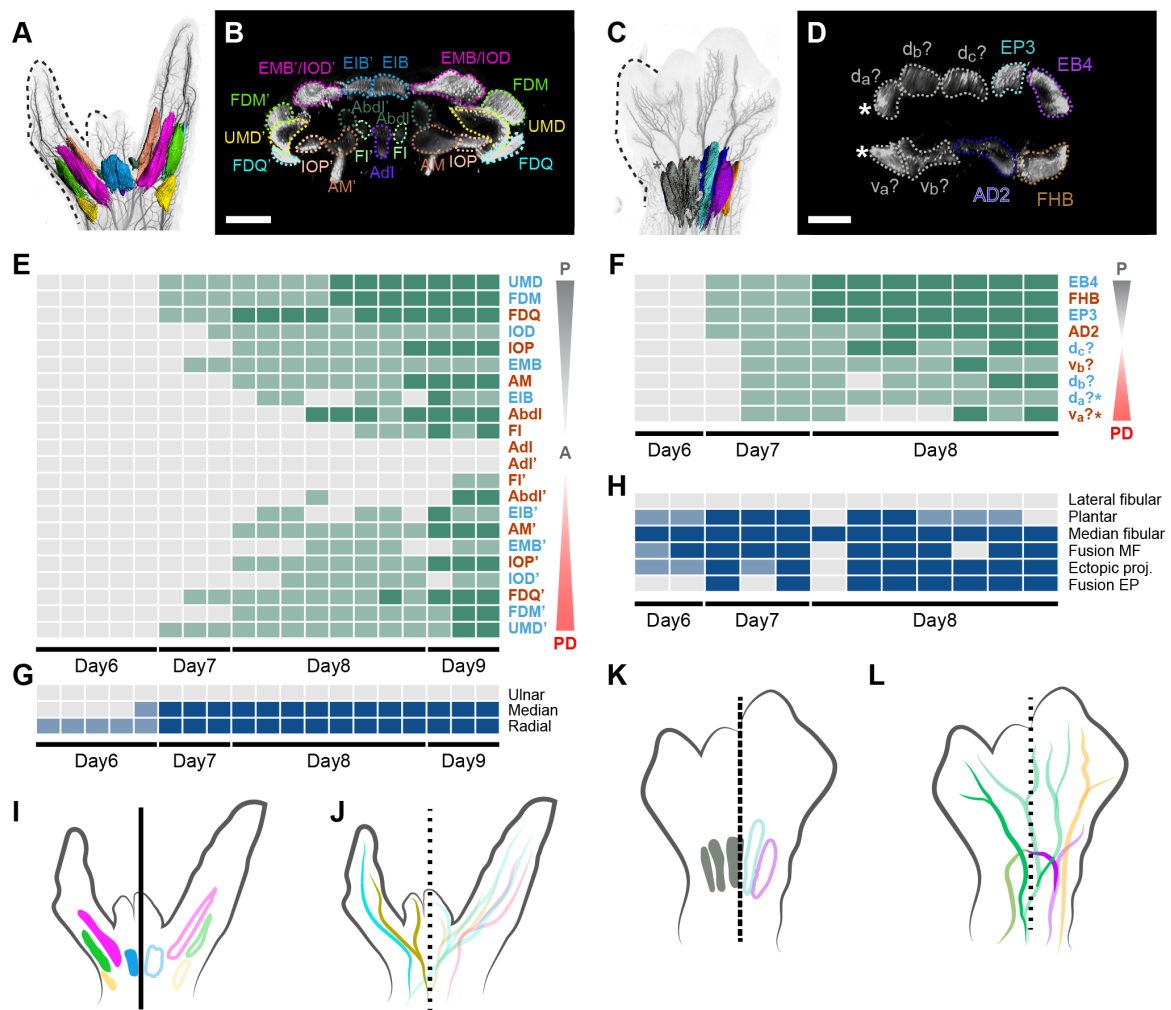
Figure 5: Differential response of muscle and nerve patterning to wing and leg polydactylies

(A-D) Full mirror-duplication of the wing musculature (A,B), and extra dorsal and ventral muscle bundles matching the single supernumerary digit in the foot (C,D). (A,B) Dorsal view (A) and virtual cross section (B) of the musculature in a polydactyl wing at day 9 of development. Muscle identity is indicated by pseudo-coloration of muscles groups. (C,D) Dorsal view (C) and virtual cross section (D) of the musculature in a polydactyl leg at day 8 of development. Identifiable muscles are indicated by pseudo-coloration, supernumerary muscles marked with an asterisk. (E-H) Temporal and spatial appearance of muscle (E,F) and nerve (G,H) pattern alterations. Dorsal (light blue) and ventral (maroon) muscles are arranged top to bottom, from posterior-native, to anterior, to polydactyl side. Muscle masses are scored as partially split (light green) or completely individualized (dark green), nerve alterations (e.g. bifurcations) as partial (light blue) or complete (dark blue, see Material and Methods for details). (I-L) Schematics of muscle and innervation patterns in polydactyl wings (I,J) and legs (K,L). While muscle patterns are completely mirror-duplicated (I, continuous line), or

21

480   follow the underlying skeletal topology (K, broken line), nerves are only partially responsive

481   (J,L, dotted lines). Only two wing nerves, median (yellow) and radial (cyan), out of three

482   show alterations (J, solid colors). Likewise, only the median fibular (green) and plantar

483   (purple) show changes in morphology (L, solid colors). Moreover, we observe the emergence

484   of an ectopic projection (olive green) joining the plantar nerve. A/P, anterior/posterior, PD,

485   polydactyl. For muscle abbreviations, refer to Fig. S3. Scale bars represent approx. 500μm.

486

487

488

489
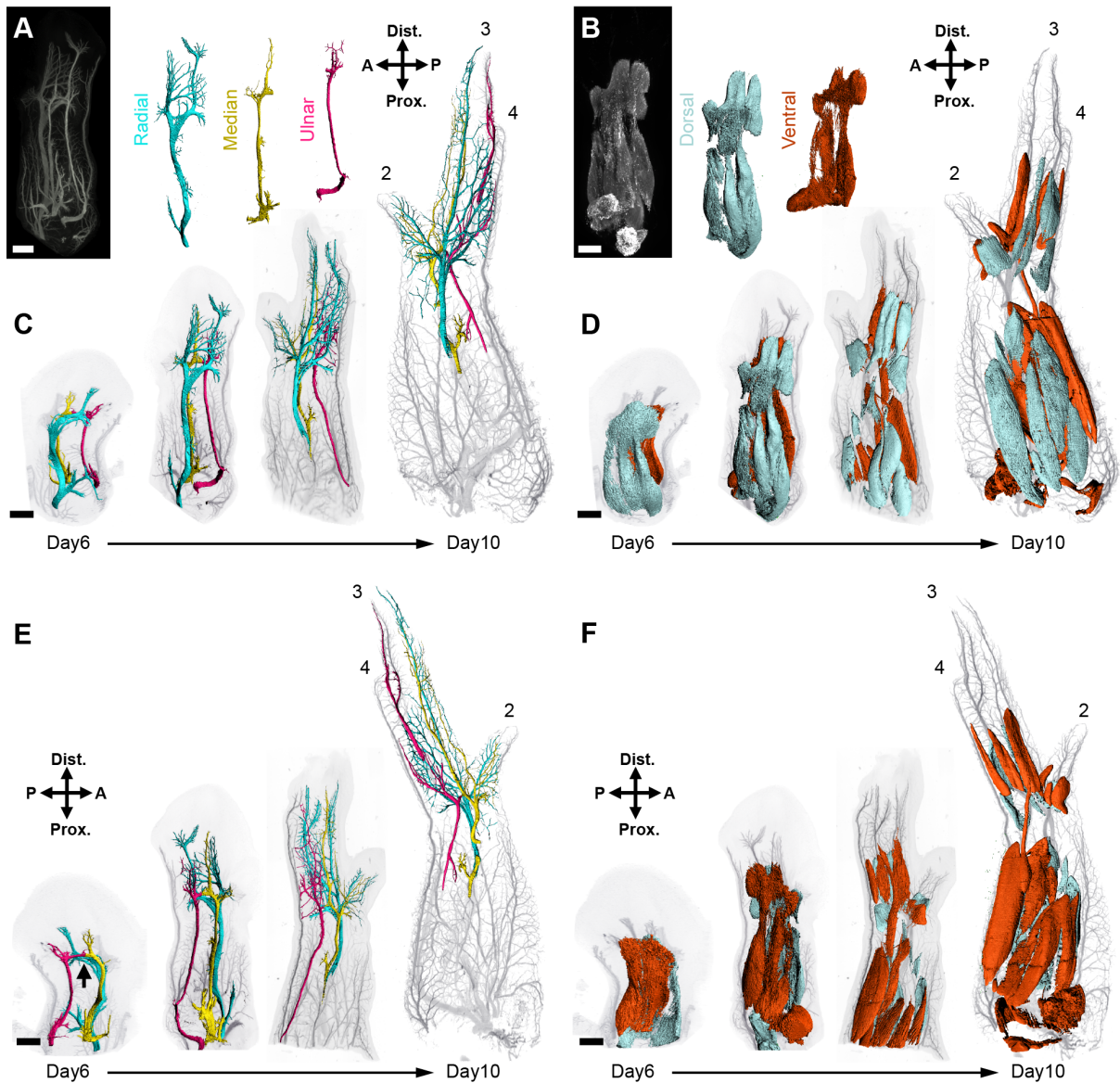
Figure S1: 3D analysis of the developing neuromuscular system in the chicken wing

(A-D) Workflow and dorsal view of the developing wing neuromuscular system. To allow for better comparisons of the dorsal and ventral halves, panels of Fig. 1 are reproduced here. (E) Ventral view of the developing wing neuromuscular system. The two main ventral nerves, the median (yellow) and ulnar (magenta), are joining together to form an arched structure (arrow) before projecting to the digits. The ulnar n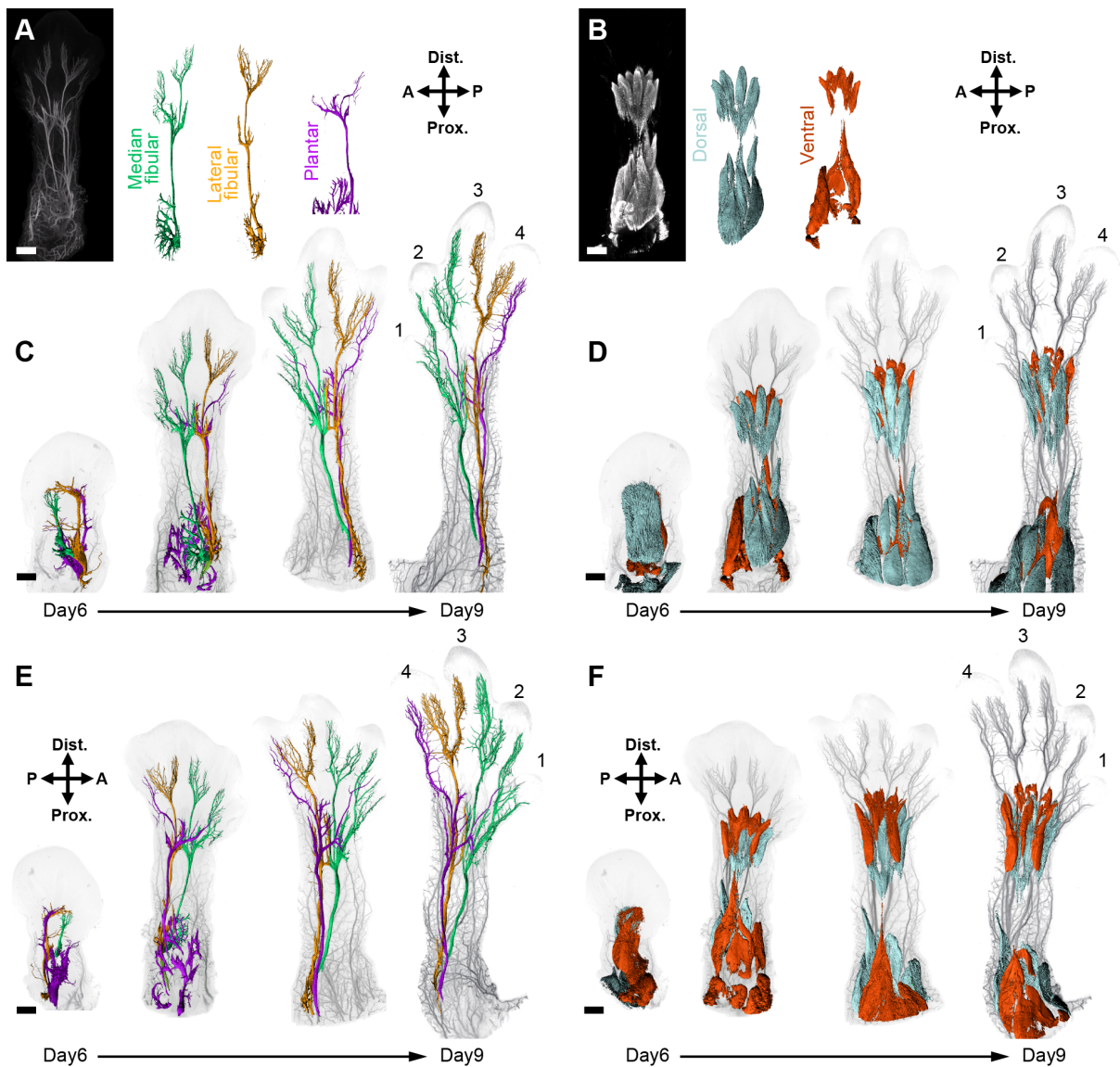erve innervates digit 4 and the median digit 2 and 3. (F) In the ventral muscle masses (red), autopodial muscles are separating from the forearm muscles at a slightly later stage than in dorsal. A/P, anterior/posterior, Prox./Dist., proximal/distal. Scale bars represent approx. 500μm.

Figure S2: 3D analysis of the developing neuromuscular system in the chicken leg

(A,B) Images showing the workflow for image analysis of lighsheet microscope data. As described in Figure 1, nerves and muscles were stained (*NF200* and *MF20*) then surfaces were created to highlight the structures of interest. (C,D) Dorsal view of the developing leg neuromuscular system. Like in the wing, three main nerves are observed: median fibular (green) and lateral fibular (orange) in dorsal, innervating the dorsal muscle masses (light blue) and plantar (violet) in ventral, connecting to the ventral muscles (red). The median and lateral fibular nerves are joining together and form an arc, similarly to the median and ulnar nerves in wing. (E,F) Ventral view of the developing leg neuromuscular system. The plantar nerve alone innervates all ventral muscles by turning from posterior to anterior. A/P, anterior/posterior, Prox./Dist., proximal/distal. Scale bars represent approx. 500μm.
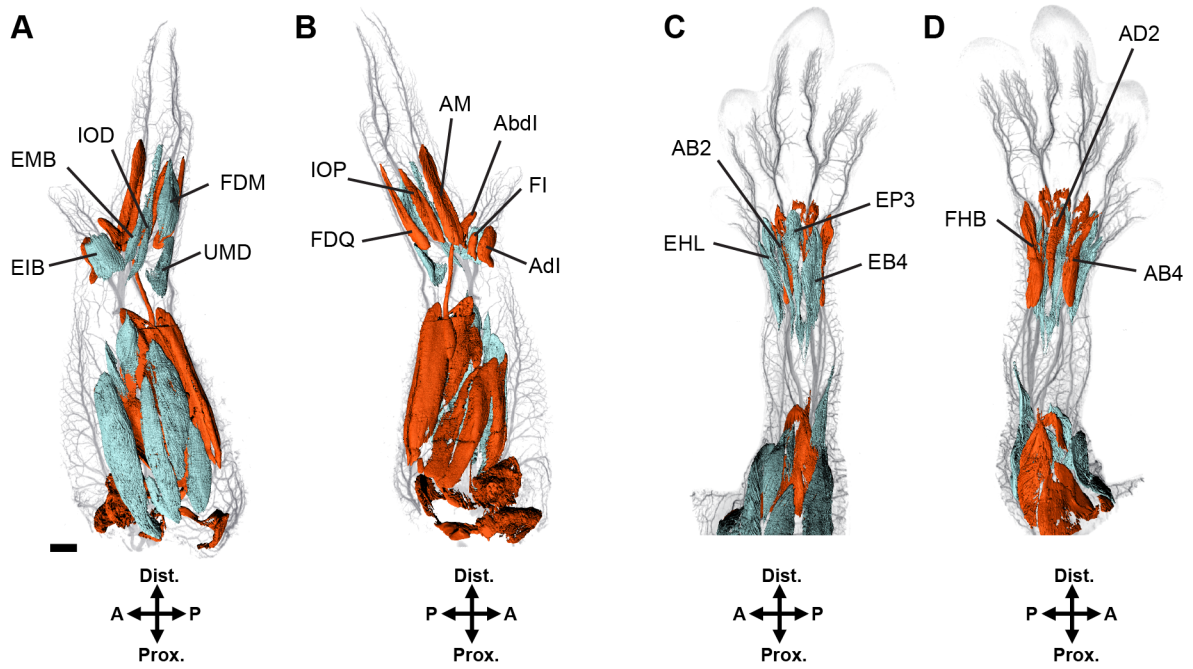
Figure S3: Autopod muscle nomenclature

(A) Wing dorsal muscles - EIB: Extensor indicis brevis; EMB: Extensor medius brevis; IOD: Interosseus dorsalis; FDM: Flexor digiti minori, UMD: Ulnimetacarpalis dorsalis. (B) Wing ventral muscles - AdI: Adductor indicis; FI: Flexor indicis; AbI: Abductor indicis; AM: Abductor medius; IOP: Interosseus palmaris; FDQ: Flexor digiti quarti. (C) Foot dorsal muscles - EHL: Extensor hallucis longus; AB2: Abductor digit 2; EP3: Extensor propius 3; EB4: Extensor brevis digit 4. (D) Foot ventral muscles - FHB: Flexor halluces brevis; AD2: Abductor digit 2; AB4: Abductor digit 4. Muscle nomenclature is based on (Sullivan, 1962) and (Kardon, 1998). A/P, anterior/posterior, Prox./Dist., proximal/distal. Scale bars represent approx. 500µm.
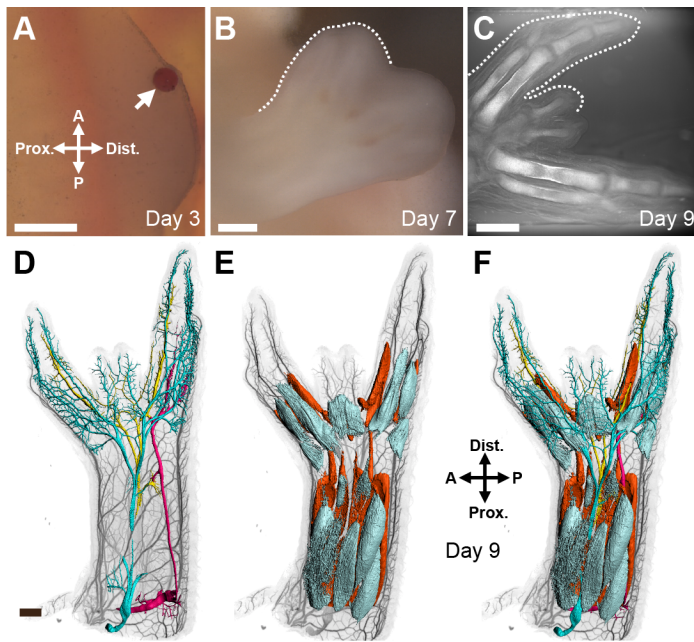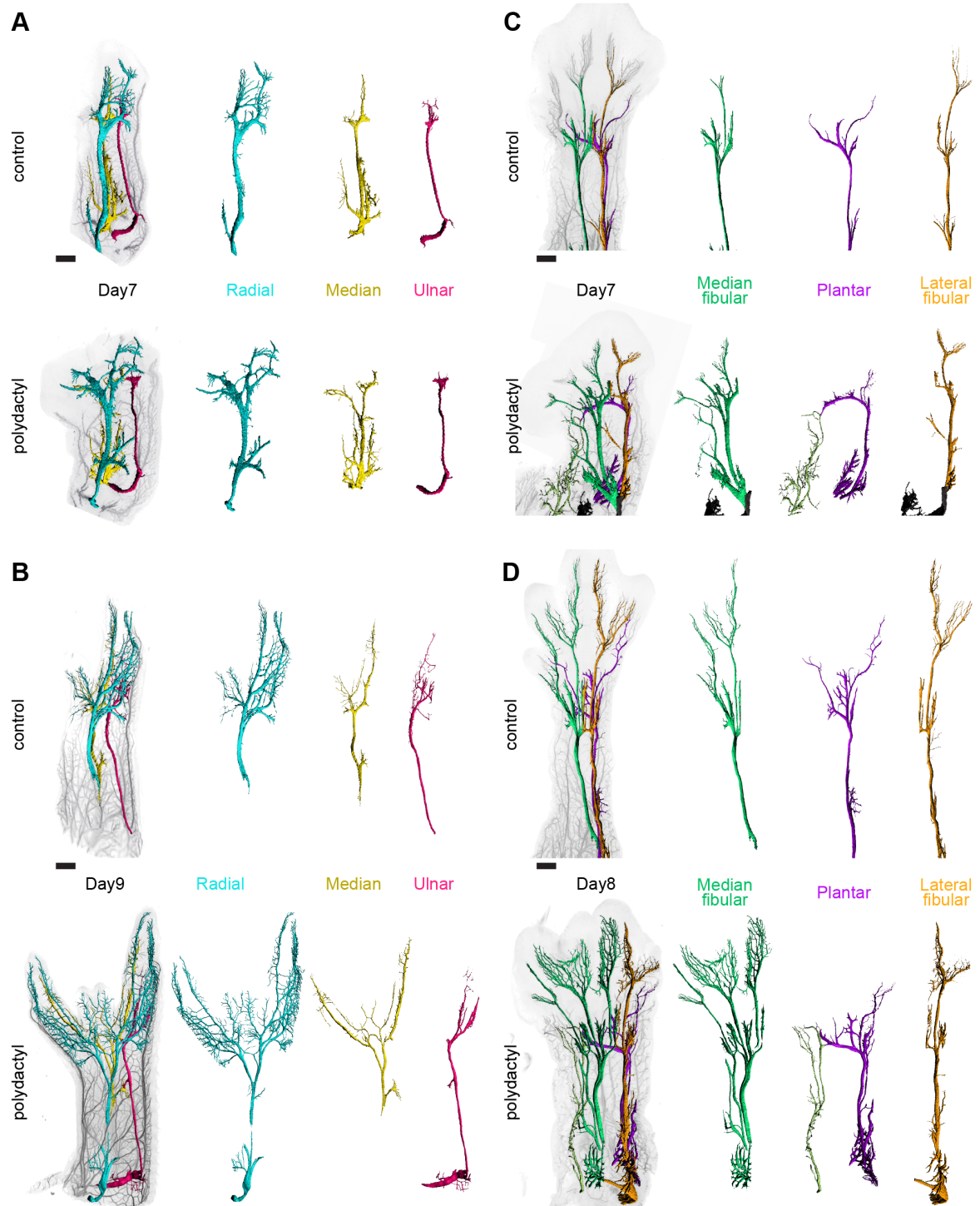
Figure S4: Generating complete mirror digit duplications

(A) Implantation of a RA-soaked bead (arrow), in the sub-AER mesenchyme of an anterior wing bud at day 3. (B) Four days after bead implantation, a mirror duplication of the wing is observed (dotted line). (C) Bright field image after CUBIC clearing reveals a complete digit mirror duplication (dotted line) at the skeletal level at day 9. (D-F) Dorsal view of innervation (D) and muscular (E) patterns, visualized in the same polydactyl wing at day 9 (F). A/P, anterior/posterior, Prox./Dist., proximal/distal. Scale bars represent approx. 500μm.

A

control

Day7 Radial Median Ulnar

polydactyl

B

control

Day9 Radial Median Ulnar

polydactyl

C

control

Day7 Median fibular Plantar Lateral fibular

polydactyl
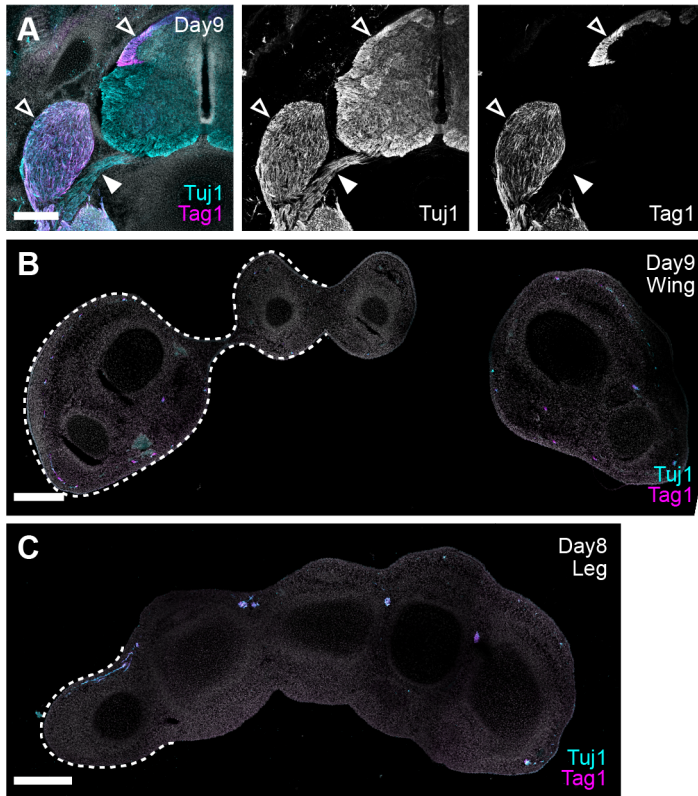
D

control

Day8 Median fibular Plantar Lateral fibular

polydactyl

Figure S5: Comparison of innervation patterns in control and polydactyl limbs

(A-D) Side-by-side comparisons of innervation patterns for control (top) and polydactyl (bottom) wings (A,B) and legs (C,D) at day 7 (A,C) and day 9 (B,D) of development. Scale bars represent approx. 500μm.

548

549 **Figure S6: Distinguishing motor and sensory nerves**

550 (A) Double-immunohistochemistry for *Tuj1* (pan-neuronal) and *Tag-1* (sensory neurons).

551 At brachial levels of the developing spinal cord, *Tag-1* marks entering sensory nerves as well

552 as the dorsal root ganglion (empty arrowheads). *Tuj1*, however, stains all neuronal structures,

553 including *Tag-1*-negative motor axons exiting ventrally from the lateral motor column to

554 project to the limb periphery (arrowhead). (B,C) At distal levels, i.e. past the autopod

555 musculature, only *Tuj1/ Tag-1* double-positive nerves are detected, both in the wing (B) as

556 well as the leg (C).

557

558

559

560   **Movie 1**: 3D-atlas of the developing neuromuscular system in chicken wings between day 6

561   and day 10 of development. Scale bar represents approx. 1mm.

562

563   **Movie 2**: 3D-atlas of the developing neuromuscular system in chicken legs between day 6

564   and day 9 of development.

565

566   **Movie 3**: Side by side comparison of wing and leg innervation patterns on virtual cross

567   sections. Abbreviation: A – anterior, P – posterior, D - dorsal, V – ventral.

568

569

REFERENCES

Askari, M., Christensen, K. N., Heath, S., Moran, S. L. and Lachman, N. (2016). Presentation of soft tissue anatomy of mirror hand: an anatomical case report with implications for surgical planning. *Surg Radiol Anat* **38**, 855–862.

Belle, M., Godefroy, D., Couly, G., Malone, S. A., Collier, F., Giacobini, P. and Chédotal, A. (2017). Tridimensional Visualization and Analysis of Early Human Development. *Cell* **169**, 161-173.e12.

Bininda-Emonds, O. R., Jeffery, J. E., Sánchez-Villagra, M. R., Hanken, J., Colbert, M., Pieau, C., Selwood, L., ten Cate, C., Raynaud, A., Osabutey, C. K., et al. (2007). Forelimb-hindlimb developmental timing changes across tetrapod phylogeny. *BMC Evol Biol* **7**, 182.

Bonanomi, D. (2019). Axon pathfinding for locomotion. *Seminars in Cell & Developmental Biology* **85**, 26–35.

Chevallier, A., Kieny, M. and Mauger, A. (1977). Limb-somite relationship: origin of the limb musculature. *Development* **41**, 245–258.

Cooper, K. L. (2011). The Lesser Egyptian Jerboa, *Jaculus jaculus* : A Unique Rodent Model for Evolution and Development: Figure 1. *Cold Spring Harbor Protocols* **2011**, pdb.emo066704.

Cooper, K. L., Sears, K. E., Uygur, A., Maier, J., Baczkowski, K.-S., Brosnahan, M., Antczak, D., Skidmore, J. A. and Tabin, C. J. (2014). Patterning and post-patterning modes of evolutionary digit loss in mammals. *Nature* **511**, 41–45.

Davey, M. G., Towers, M., Vargesson, N. and Tickle, C. (2018). The chick limb: embryology, genetics and teratology. *The International Journal of Developmental Biology* **62**, 85–95.

de Bakker, M. A. G., Fowler, D. A., Oude, K. den, Dondorp, E. M., Navas, M. C. G., Horbanczuk, J. O., Sire, J.-Y., Szczerbińska, D. and Richardson, M. K. (2013). Digit loss in archosaur evolution and the interplay between selection and constraints. *Nature* **500**, 445–448.

di Sanguinetto, S. A. D. T., Dasen, J. S. and Arber, S. (2008). Transcriptional mechanisms controlling motor neuron diversity and connectivity. *Current Opinion in Neurobiology* **18**, 36–43.

Diogo, R., Walsh, S., Smith, C., Ziermann, J. M. and Abdala, V. (2015). Towards the resolution of a long-standing evolutionary question: muscle identity and attachments are mainly related to topological position and not to primordium or homeotic identity of digits. *J Anat* **226**, 523–529.

Duprez, D., Lapointe, F., Edom-Vovard, F., Kostakopoulou, K. and Robson, L. (1999). Sonic Hedgehog (SHH) specifies muscle pattern at tissue and cellular chick level, in the chick limb bud. *Mechanisms of Development* **82**, 151–163.

Francisco Botelho, J., Smith-Paredes, D., Soto-Acuña, S., Mpodozis, J., Palma, V. and Vargas, A. O. (2015). Skeletal plasticity in response to embryonic muscular activity underlies the development and evolution of the perching digit of birds. *Scientific Reports* **5**, 9840.

Friocourt, F., Lafont, A.-G., Kress, C., Pain, B., Manceau, M., Dufour, S. and Chédotal, A. (2017). Recurrent *DCC* gene losses during bird evolution. *Scientific Reports* **7**, 37569.

Gilbert, S. F. (2010). *Developmental Biology*. Sinauer Associates.

Gouti, M., Metzis, V. and Briscoe, J. (2015). The route to spinal cord cell types: a tale of signals and switches. *Trends in Genetics* **31**, 282–289.

Hall, B. K. ed. (2015). Front-matter. In *Bones and Cartilage (Second Edition)*, pp. i–iii. San Diego: Academic Press.

620 **Hamburger, V. and Hamilton, H. L.** (1951). A series of normal stages in the development
621 of the chick embryo. *J. Morphol.* **88**, 49–92.
622 **Hayashi, K. and Ozawa, E.** (1995). Myogenic cell migration from somites is induced by
623 tissue contact with medial region of the presumptive limb mesoderm in chick embryos.
624 *Development* **121**, 661–669.
625 **Huang, A. H., Riordan, T. J., Pryce, B., Weibel, J. L., Watson, S. S., Long, F., Lefebvre,**
626 **V., Harfe, B. D., Stadler, H. S., Akiyama, H., et al.** (2015). Musculoskeletal integration at
627 the wrist underlies the modular development of limb tendons. *Development* **142**, 2431–2441.
628 **Karagogeos, D., Pourquié, C., Kyriakopoulou, K., Tavian, M., Stallcup, W., Péault, B.**
629 **and Pourquié, O.** (1997). Expression of the cell adhesion proteins BEN/SC1/DM-GRASP
630 and TAG-1 defines early steps of axonogenesis in the human spinal cord. *Journal of*
631 *Comparative Neurology* **379**, 415–427.
632 **Kardon, G.** (1998). Muscle and tendon morphogenesis in the avian hind limb. *Development*
633 **125**, 4019–4032.
634 **Kronenberg, H. M.** (2003). Developmental regulation of the growth plate. *Nature* **423**, 332–
635 336.
636 **Lance-Jones, C. and Landmesser, L.** (1981). Pathway selection by embryonic chick
637 motoneurons in an experimentally altered environment. *Proc. R. Soc. Lond., B, Biol. Sci.* **214**,
638 19–52.
639 **Landmesser, L.** (1978). The development of motor projection patterns in the chick hind
640 limb. *J Physiol* **284**, 391–414.
641 **Landmesser, L. T.** (2001). The acquisition of motoneuron subtype identity and motor circuit
642 formation. *Int. J. Dev. Neurosci.* **19**, 175–182.
643 **Lettice, L. A., Hill, A. E., Devenney, P. S. and Hill, R. E.** (2008). Point mutations in a
644 distant sonic hedgehog cis-regulator generate a variable regulatory output responsible for
645 preaxial polydactyly. *Human Molecular Genetics* **17**, 978–985.
646 **Lopez-Rios, J., Duchesne, A., Speziale, D., Andrey, G., Peterson, K. A., Germann, P.,**
647 **Unal, E., Liu, J., Floriot, S., Barbey, S., et al.** (2014). Attenuated sensing of SHH by Ptch1
648 underlies evolution of bovine limbs. *Nature* **511**, 46–51.
649 **Mehring, C., Akselrod, M., Bashford, L., Mace, M., Choi, H., Blüher, M., Buschhoff, A.-**
650 **S., Pistohl, T., Salomon, R., Cheah, A., et al.** (2019). Augmented manipulation ability in
651 humans with six-fingered hands. *Nature Communications* **10**, 2401.
652 **Petit, F., Sears, K. E. and Ahituv, N.** (2017). Limb development: a paradigm of gene
653 regulation. *Nature Reviews Genetics* **18**, 245–258.
654 **Pickering, J., Wali, N. and Towers, M.** (2017). Transcriptional changes in chick wing bud
655 polarization induced by retinoic acid. *Developmental Dynamics* **246**, 682–690.
656 **Preibisch, S., Saalfeld, S. and Tomancak, P.** (2009). Globally optimal stitching of tiled 3D
657 microscopic image acquisitions. *Bioinformatics* **25**, 1463–1465.
658 **Richardson, M. K. and Chipman, A. D.** (2003). Developmental constraints in a
659 comparative framework: A test case using variations in phalanx number during amniote
660 evolution. *Journal of Experimental Zoology Part B: Molecular and Developmental Evolution*
661 **296B**, 8–22.
662 **Ros, M. A., Kay Simandl, B., Clark, A. W. and Fallon, J. F.** (2000). Methods for
663 Manipulating the Chick Limb Bud to Study Gene Expression, Tissue Interactions, and
664 Patterning. In *Developmental Biology Protocols* (ed. Tuan, R. S.) and Lo, C. W.), pp. 245–
665 266. Totowa, NJ: Humana Press.
666 **Ruegg, M. A., Stoeckli, E. T., Kuhn, T. B., Heller, M., Zuellig, R. and Sonderegger, P.**
667 (1989). Purification of axonin-1, a protein that is secreted from axons during neurogenesis.
668 *The EMBO Journal* **8**, 55–63.

669 **Schindelin, J., Arganda-Carreras, I., Frise, E., Kaynig, V., Longair, M., Pietzsch, T.,**
670 **Preibisch, S., Rueden, C., Saalfeld, S., Schmid, B., et al.** (2012). Fiji - an Open Source
671 platform for biological image analysis. *Nat Methods* **9**,.
672 **Schramm, C. and Solursh, M.** (1990). The formation of premuscle masses during chick
673 wing bud development. *Anat. Embryol.* **182**, 235–247.
674 **Schweitzer, R., Zelzer, E. and Volk, T.** (2010). Connecting muscles to tendons: tendons and
675 musculoskeletal development in flies and vertebrates. *Development* **137**, 2807–2817.
676 **Shapiro, M. D., Hanken, J. and Rosenthal, N.** (2003). Developmental basis of evolutionary
677 digit loss in the Australian lizard Hemiergis. *J. Exp. Zool. B Mol. Dev. Evol.* **297**, 48–56.
678 **Sharir, A., Stern, T., Rot, C., Shahar, R. and Zelzer, E.** (2011). Muscle force regulates
679 bone shaping for optimal load-bearing capacity during embryogenesis. *Development* **138**,
680 3247–3259.
681 **Shubin, N., Tabin, C. and Carroll, S.** (1997). Fossils, genes and the evolution of animal
682 limbs. *Nature* **388**, 639.
683 **Stirling, R. V. and Summerbell, D.** (1988). Specific guidance of motor axons to duplicated
684 muscles in the developing amniote limb. *Development* **103**, 97–110.
685 **Sullivan, G.** (1962). Anatomy and embryology of the Wing Musculature of the domestic
686 fowl (gallus). *Australian Journal of Zoology* **10**, 458.
687 **Susaki, E. A., Tainaka, K., Perrin, D., Kishino, F., Tawara, T., Watanabe, T. M.,**
688 **Yokoyama, C., Onoe, H., Eguchi, M., Yamaguchi, S., et al.** (2014). Whole-Brain Imaging
689 with Single-Cell Resolution Using Chemical Cocktails and Computational Analysis. *Cell*
690 **157**, 726–739.
691 **Susaki, E. A., Tainaka, K., Perrin, D., Yukinaga, H., Kuno, A. and Ueda, H. R.** (2015).
692 Advanced CUBIC protocols for whole-brain and whole-body clearing and imaging. *Nature*
693 *Protocols* **10**, 1709–1727.
694 **Suzuki, T.** (2013). How is digit identity determined during limb development? *Dev. Growth*
695 *Differ.* **55**, 130–138.
696 **Tickle, C. and Towers, M.** (2017). Sonic Hedgehog Signaling in Limb Development. *Front*
697 *Cell Dev Biol* **5**,.
698 **Tickle, C., Alberts, B., Wolpert, L. and Lee, J.** (1982). Local application of retinoic acid to
699 the limb bond mimics the action of the polarizing region. *Nature* **296**, 564–566.
700 **Tickle, C., Lee, J. and Eichele, G.** (1985). A quantitative analysis of the effect of all-trans-
701 retinoic acid on the pattern of chick wing development. *Developmental Biology* **109**, 82–95.
702 **Tschopp, P., Sherratt, E., Sanger, T. J., Groner, A. C., Aspiras, A. C., Hu, J. K.,**
703 **Pourquié, O., Gros, J. and Tabin, C. J.** (2014). A relative shift in cloacal location
704 repositions external genitalia in amniote evolution. *Nature* **516**, 391–394.
705 **Vallecillo-García, P., Orgeur, M., Hofe-Schneider, S. vom, Stumm, J., Kappert, V.,**
706 **Ibrahim, D. M., Börno, S. T., Hayashi, S., Relaix, F., Hildebrandt, K., et al.** (2017). Odd
707 skipped-related 1 identifies a population of embryonic fibro-adipogenic progenitors
708 regulating myogenesis during limb development. *Nature Communications* **8**, 1218.
709 **Wagner, G. P.** (2014). *Homology, Genes, and Evolutionary Innovation*. Princeton University
710 Press.
711 **Wagner, G. P. and Chiu, C. H.** (2001). The tetrapod limb: a hypothesis on its origin. *J. Exp.*
712 *Zool.* **291**, 226–240.
713 **Wimsatt, W.** (2012). *Biology of Bats*. Elsevier.
714 **Young, N. M. and Hallgrímsson, B.** (2005). Serial homology and the evolution of
715 mammalian limb covariation structure. *Evolution* **59**, 2691–2704.
716 **Zeller, R., López-Ríos, J. and Zuniga, A.** (2009). Vertebrate limb bud development:
717 moving towards integrative analysis of organogenesis. *Nature Reviews Genetics* **10**, 845–858.

718   **Zuniga, A.** (2015). Next generation limb development and evolution: old questions, new
719   perspectives. *Development* **142**, 3810–3820.
720